Supplementary information for

Operando Insights on Stable Cu^{2+} Active Sites for Efficient Electrochemical CO_2-to-C_2H_4 Conversion

Zonghang Zhang, Qiang Xu, Jingwei Han, Ke Ren, Yinmeng Hu, Rui Zhao, Hai Sun, Jun-Sheng Qin*, Heng Rao*

State Key Laboratory of Inorganic Synthesis and Preparative Chemistry, College of Chemistry, International Center of Future Science, Jilin University, 2699 Qianjin Street, Changchun 130012, PR China

*Address correspondence to: qin@jlu.edu.cn; rao@jlu.edu.cn

Supplementary Figures

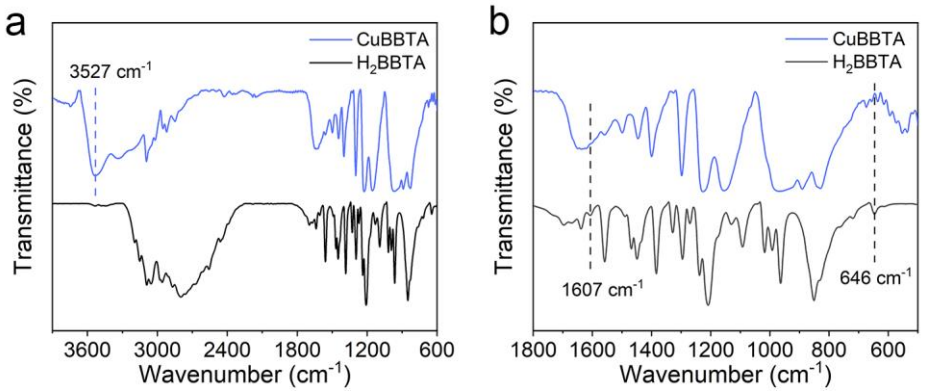

Supplementary Fig. 1 | Fourier-transform infrared spectroscopy (FT-IR). The full spectra (a) and magnified spectra of H_2BBTA and CuBBTA (b). The wide N-H stretching (from 3300 to 2600 cm^{-1}) is absent in CuBBTA. The peak at 3527 cm^{-1} in CuBBTA is attributed to the hydroxyl group.[1] The absence of N-H in-plane bending (~1607 cm^{-1}) and N-H out-of-plane bending (~646 cm^{-1}) in CuBBTA indicates that the N atom in H_2BBTA is deprotonated.[2]

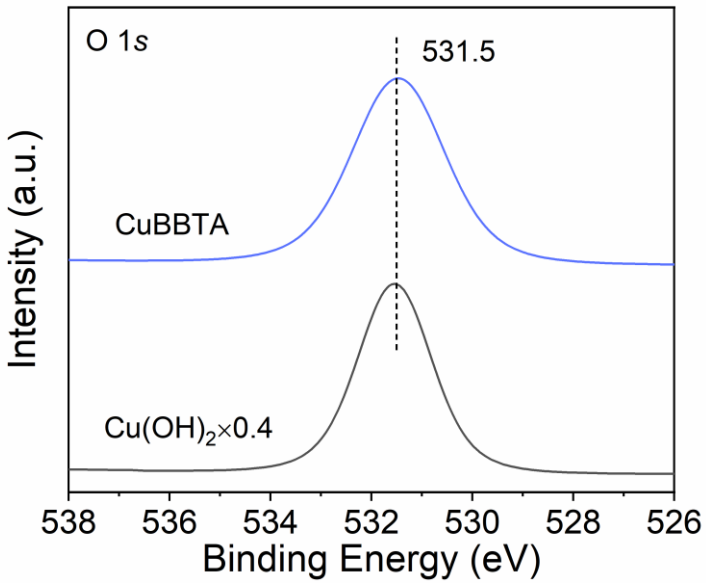

Supplementary Fig. 2 | O 1*s* XPS of CuBBTA. CuBBTA showed the same O 1*s* binding energy as that in the reference $Cu(OH)_2$ sample.

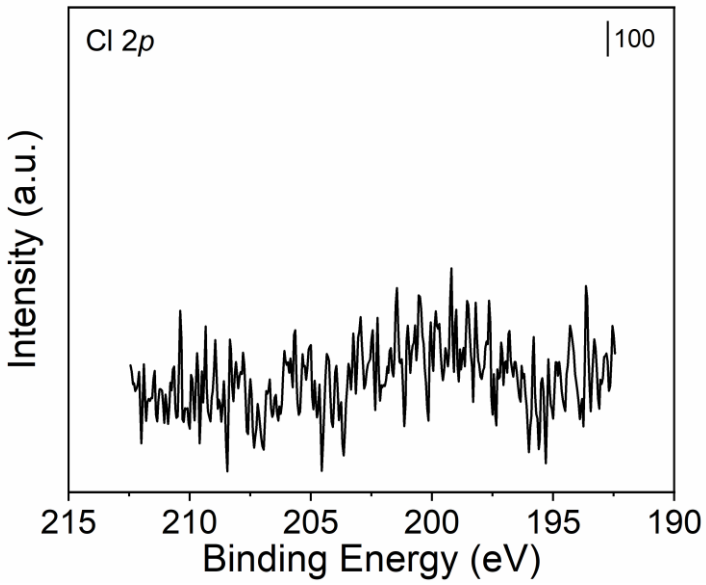

Supplementary Fig. 3 | The absence of Cl 2*p* signal illustrated that the chloride ions in the $CuCl_2$ precursor were completely replaced and did not involve coordination in CuBBTA.

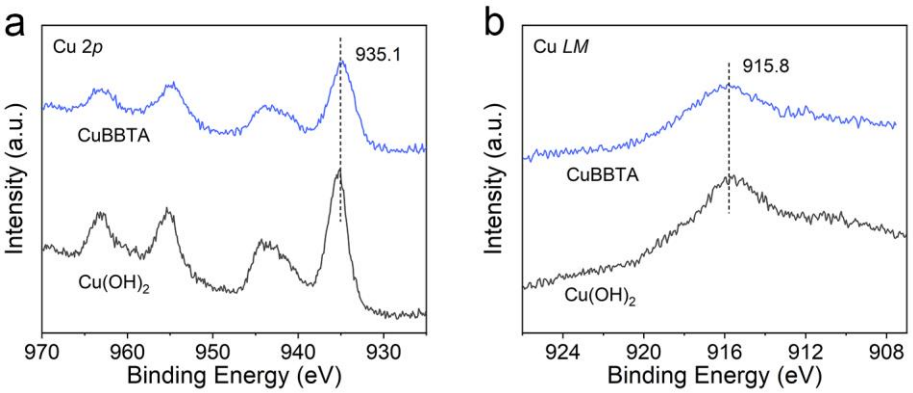

Supplementary Fig. 4 | High-resolution Cu XPS. Cu 2*p* spectra (a) and Cu *LM* spectra (b) of CuBBTA and $Cu(OH)_2$.

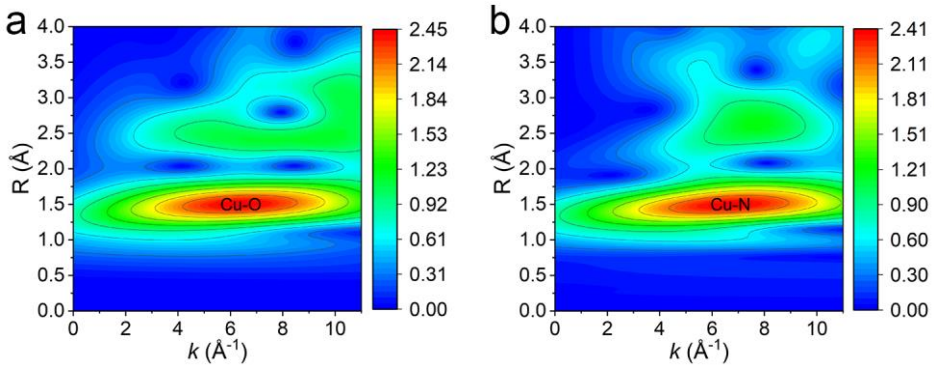

Supplementary Fig. 5 | XAFS wavelet transform (WT) for the reference samples. (a) Commercial CuO. (b) Commercial CuPc. The y-axis of the WT plots shows the radial distance, and the x-axis reflects the k-space resolution of the backscattering atom.

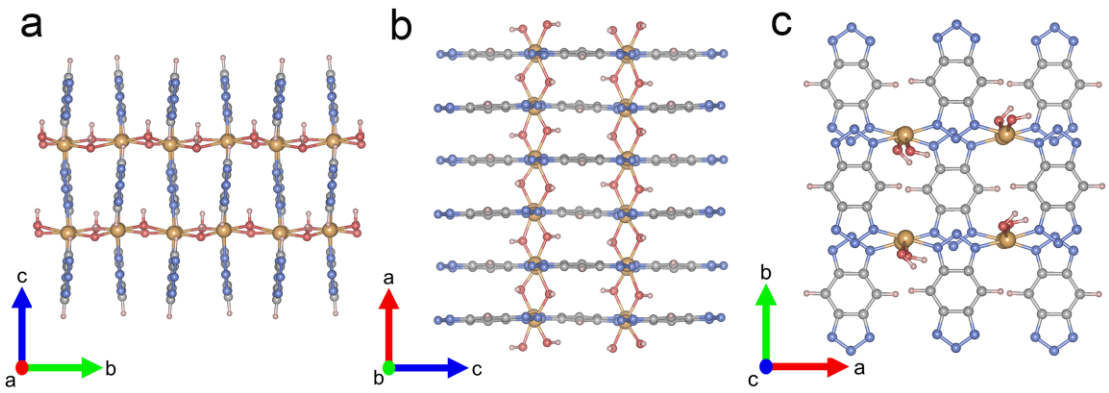

Supplementary Fig. 6 | Model of the CuBBTA. Views from the a-axis (a), b-axis (b), and c-axis (c). The calculated theoretical mass percentage of elements in CuBBTA (Calc.: Cu: 39.82%, C: 22.57%, N: 26.33%, O: 10.2%, H: 1.26%).

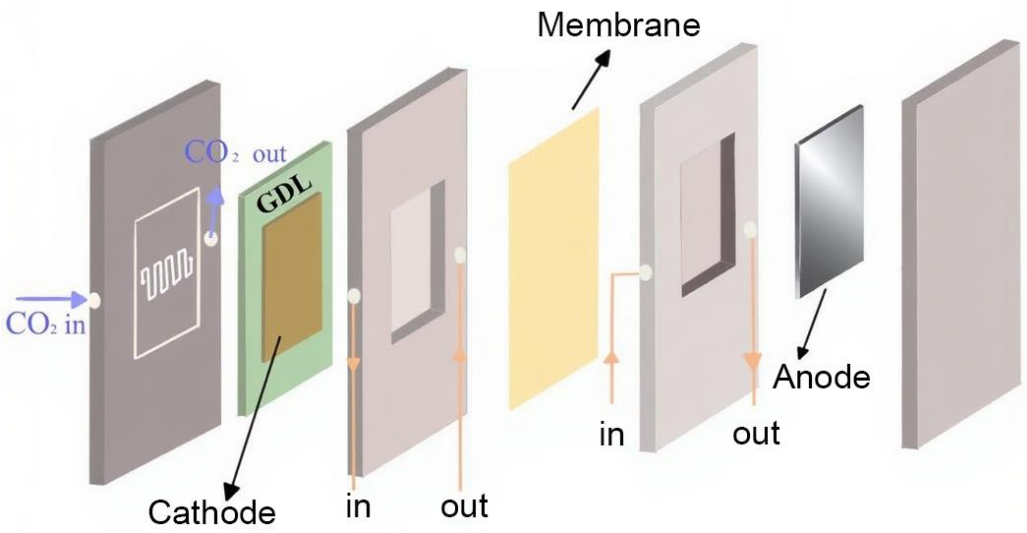

Supplementary Fig. 7 | The schematic diagram of the electrochemical flow cell.

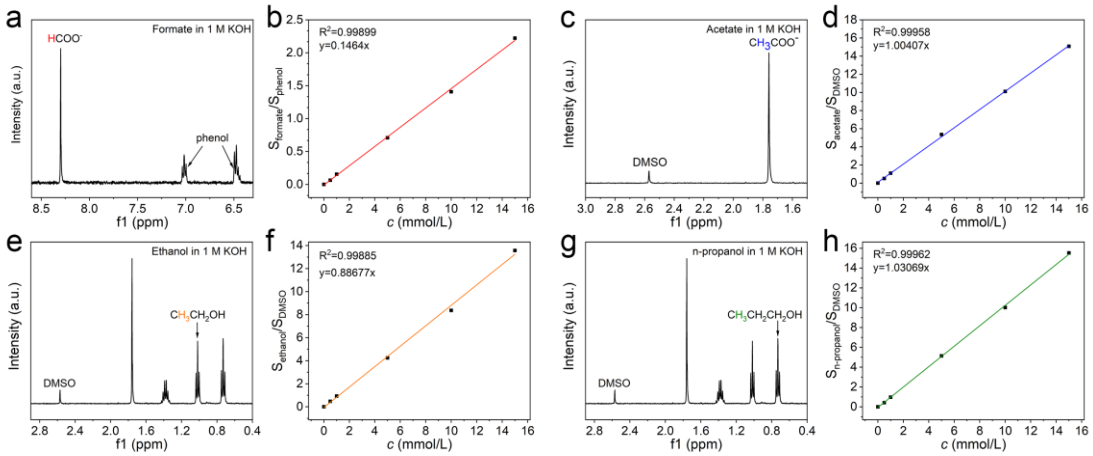

Supplementary Fig. 8 | Magnified view of the 1 H-NMR spectrum highlighting characteristic peaks of various liquid products. 1H-NMR spectrum (a) and calibration plot (b) for formate measured in 1 M KOH electrolyte. 1H-NMR spectrum (c) and calibration plot (d) for acetate measured in 1 M KOH electrolyte. 1H-NMR spectrum (e) and calibration plot (f) for ethanol measured in 1 M KOH electrolyte. 1H-NMR spectrum (g) and calibration plot (h) for n-propanol measured in 1 M KOH electrolyte. Phenol (triplet, δ=7.03) and DMSO (singlet, δ=2.6) were used as internal standards for quantification of formate and other liquid products, respectively.

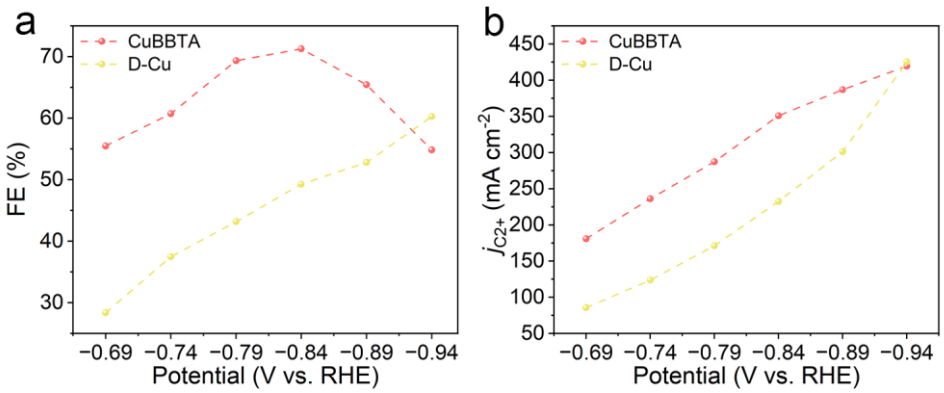

Supplementary Fig. 9 | FE and Partial current densities for C_{2+} products over CuBBTA and D-Cu catalysts.

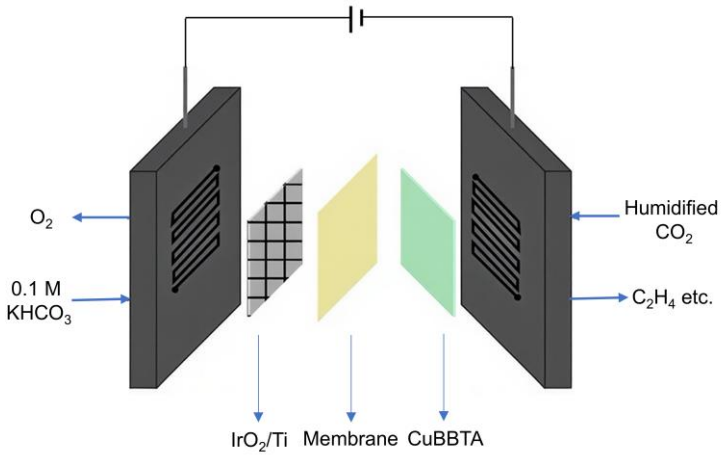

Supplementary Fig. 10 | Schematic illustration of the MEA system.

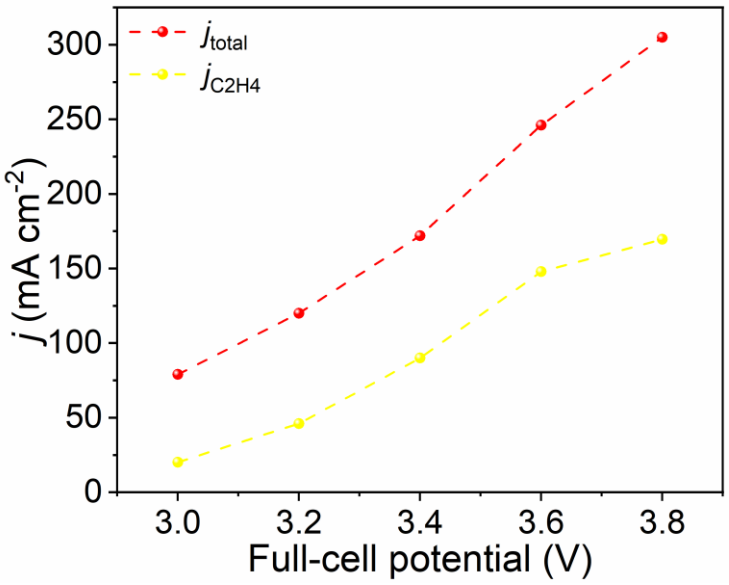

Supplementary Fig. 11 | Total current density and C_2H_4 partial current density over CuBBTA at different full-cell potentials measured in the MEA system.

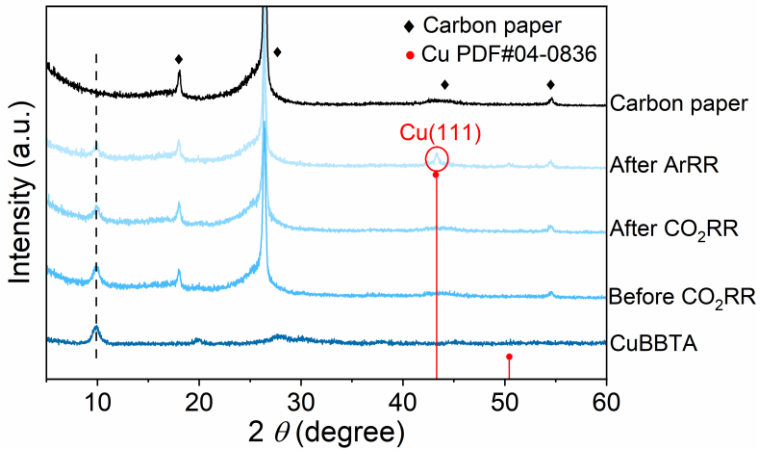

Supplementary Fig. 12 | XRD of CuBBTA, before the CO_2RR electrolysis, after the CO_2RR electrolysis, electroreduction at −300 mA cm^{-2} for 5 min under an Ar atmosphere, carbon paper. The XRD before and after the CO_2RR electrolysis was unchanged and retained the main peak of CuBBTA. The peak of Cu(111) was clearly observed after electrolysis at -300 mA cm^{-2} for 10 min under argon atmosphere.The Cu standard pattern (PDF#04-0836) was used as the reference.

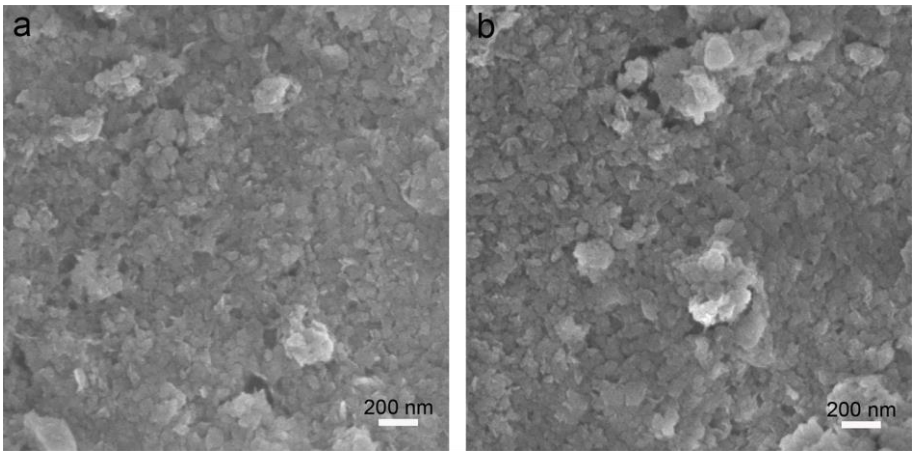

Supplementary Fig. 13 | Scanning electron microscopy (SEM) images of CuBBTA before and after stability test in the MEA system. (a) the CuBBTA on the carbon cloth before CO_2RR process. (b) the CuBBTA on the carbon cloth after CO_2RR process. The structure of CuBBTA remained the same after the stability test.

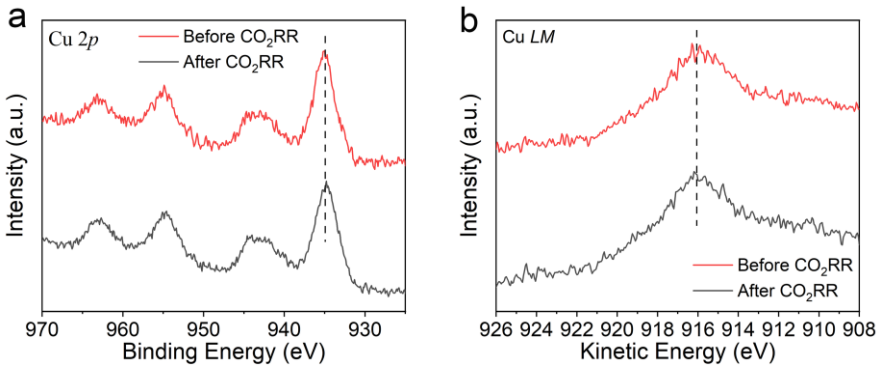

Supplementary Fig. 14 | High-resolution Cu XPS of CuBBTA before and after CO_2RR stability test. (a) Cu 2*p* spectrum. (b) Cu *LM* spectrum.

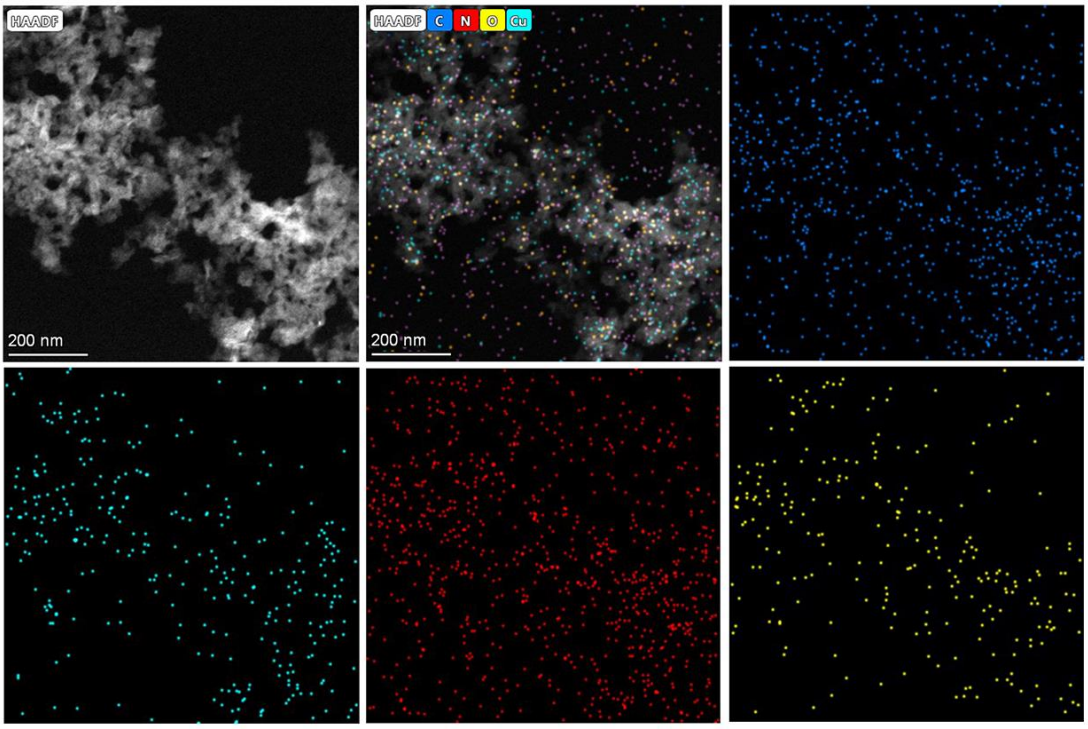

Supplementary Fig. 15 | Scanning transmission electron microscopy (STEM) elemental mapping of CuBBTA after CO_2RR stability test. No copper nanoclusters appeared.

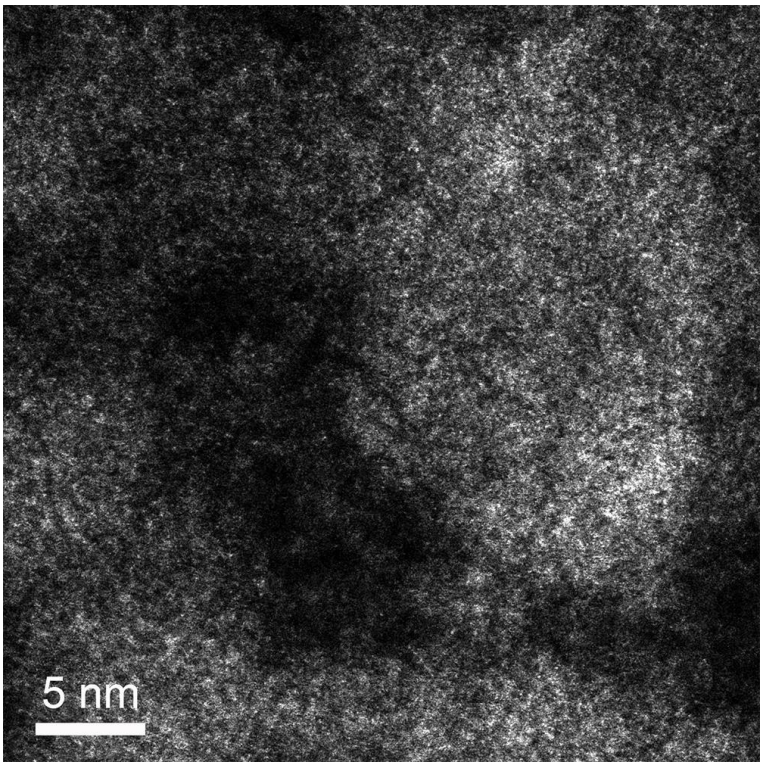

Supplementary Fig. 16 | HAADF-STEM image of CuBBTA after CO_2RR stability test. Copper is distributed as single atoms.

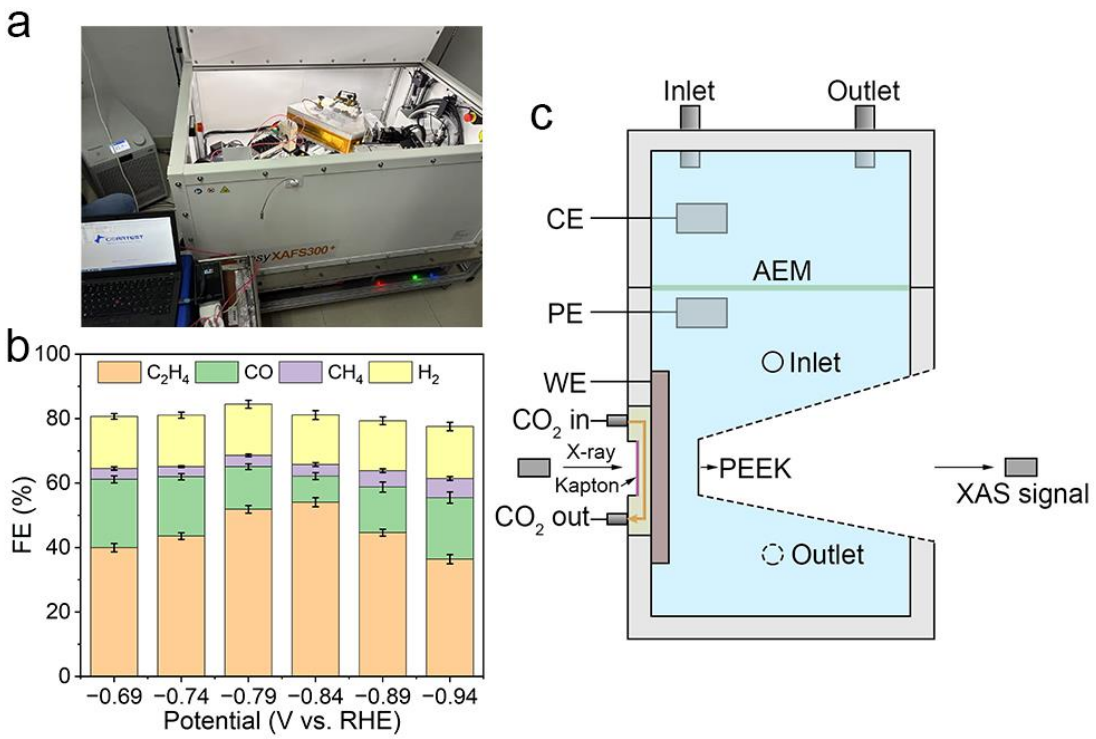

Supplementary Fig. 17 | (a) The photograph of operando XAFS (b) The CO_2RR performance of CuBBTA performed in the operando flow-cell electrolyzer (c), Illustration of in situ XAS electrochemical cells for transmittance mode.

The *operando* XAS experiments were performed using a flow cell configuration. The only modification from the flow cell employed for CO_2 reduction performance evaluation was the use of Kapton tape to seal the gas chamber, enabling X-ray irradiation and allowing fluorescent signal detection. we evaluated the CO_2 reduction reaction (CO_2RR) performance in our laboratory using the same *operando* XAS flow cell under identical experimental conditions. The Faradaic efficiencies of each gaseous product and the corresponding current densities at each applied potential were found to be nearly identical to those obtained using the standard flow cell.

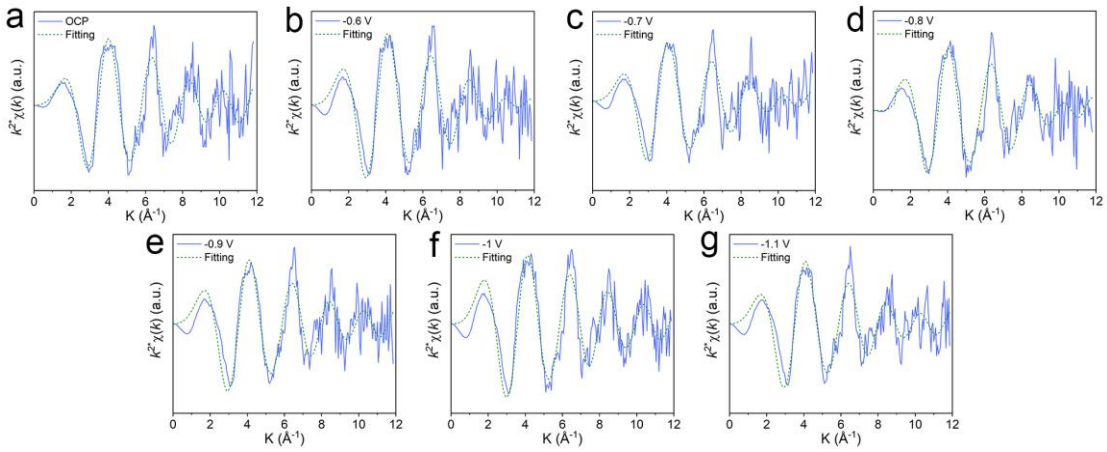

Supplementary Fig. 18 | Operando k^2-weighted Cu K-edge EXAFS spectra for CuBBTA under at representative potentials. (a) Under open-circuit voltage. (b) At -0.6 V vs. RHE. (c) At -0.7 V vs. RHE. (d) At -0.8 V vs. RHE. (e) At -0.9 V vs. RHE. (f) At -1 V vs. RHE. (g) At -1.1 V vs. RHE.

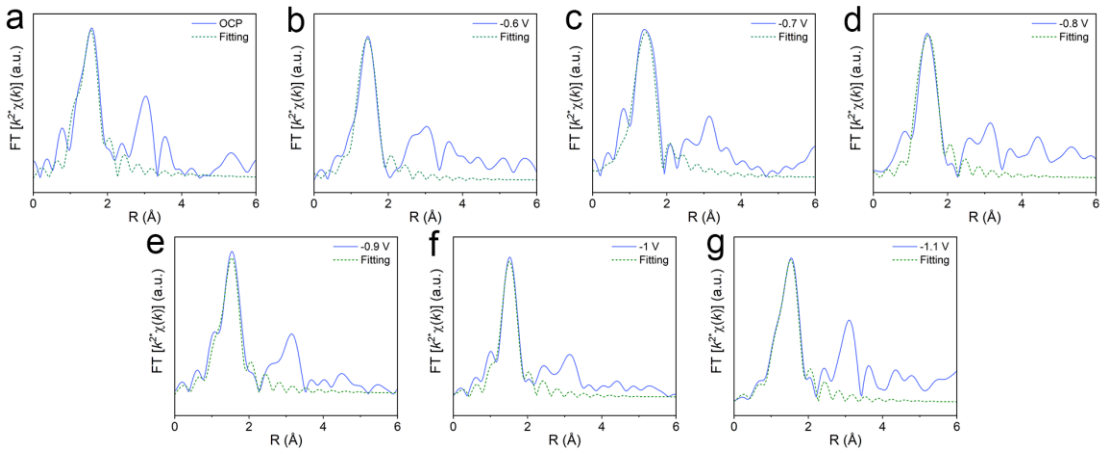

Supplementary Fig. 19 | Fourier-transformed magnitudes for CuBBTA under at representative potentials. (a) Under open-circuit voltage. (b) At -0.6 V vs. RHE. (c) At -0.7 V vs. RHE. (d) At -0.8 V vs. RHE. (e) At -0.9 V vs. RHE. (f) At -1 V vs. RHE. (g) At -1.1 V vs. RHE.

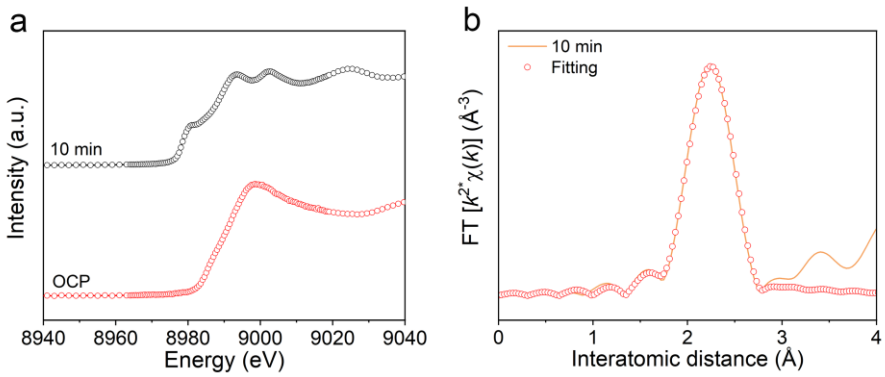

Supplementary Fig. 20 | *Operando* XAFS measurements. Cu K-edge XANES of CuBBTA catalysts at a constant current density of -300 mA cm^{-2} under Ar atmosphere. (a) Cu K-edge XANES spectra after electroreduction for 10 min. (b) The Cu K-edge EXAFS fitting spectrum of as-reduced CuBBTA after electroreduction for 10 min. The phase of metallic Cu was formatted quickly under Ar atmosphere, which was consistent with the result of XRD.

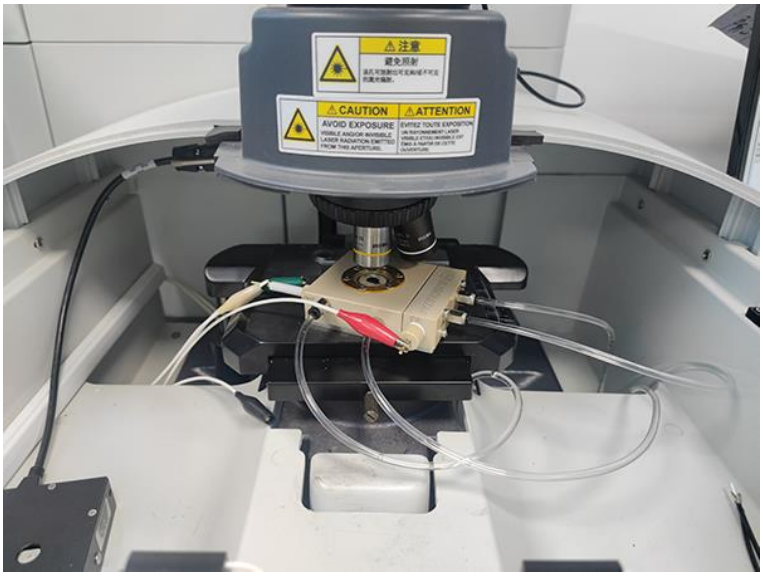

Supplementary Fig. 21 | The electrochemical cell for *Operando* Raman measurements. A water immersion objective and a 532 nm laser were used. An Ag/AgCl (saturated KCl) electrode and a Pt wire were used as the reference and counter electrodes, respectively.

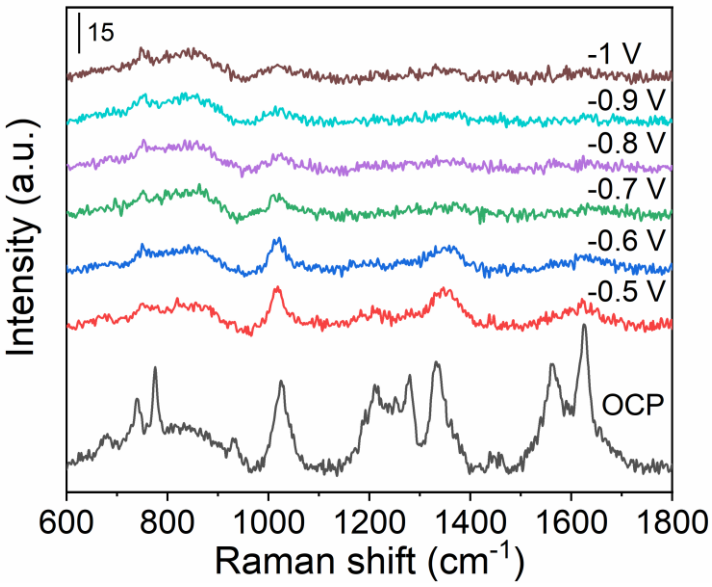

Supplementary Fig. 22 | *Operando* Raman spectra of CuBBTA at the applied potential of -0.5 V to -1 V under Ar atmosphere. At open-circuit potential (OCP), CuBBTA exhibited characteristic Raman shifts corresponding to its vibrational modes; these signals diminished with increasingly negative potentials and disappeared entirely below -0.5 V.

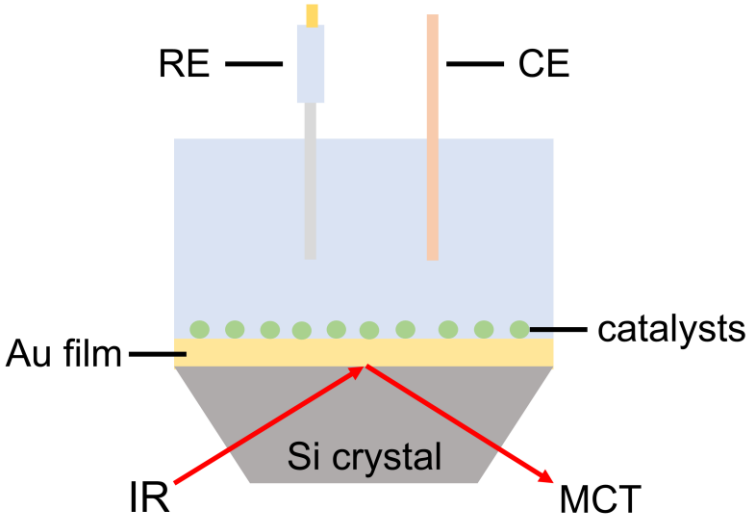

Supplementary Fig. 23 | Schematic diagram of ATR-SEIRAS device.

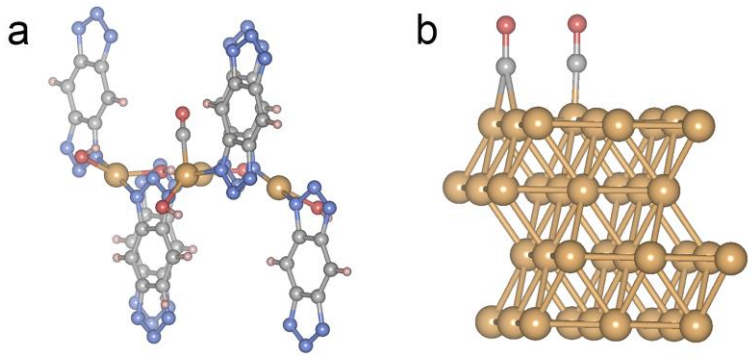

Supplementary Fig. 24 | DFT-predicted *CO intermediate configuration on CuBBTA (a) and D-Cu slab (b).

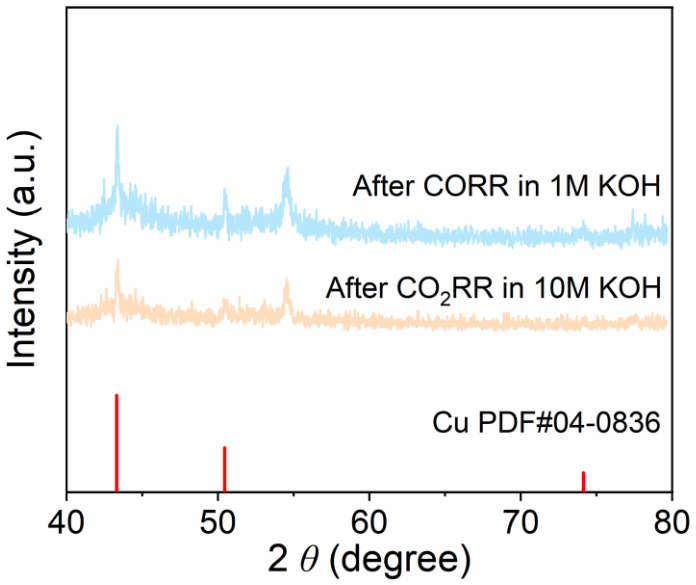

Supplementary Fig. 25 | The XRD patterns of CuBBTA after CORR measurement in 1 M KOH electrolyte and CO_2RR measurement in 10 M KOH electrolyte, respectively.

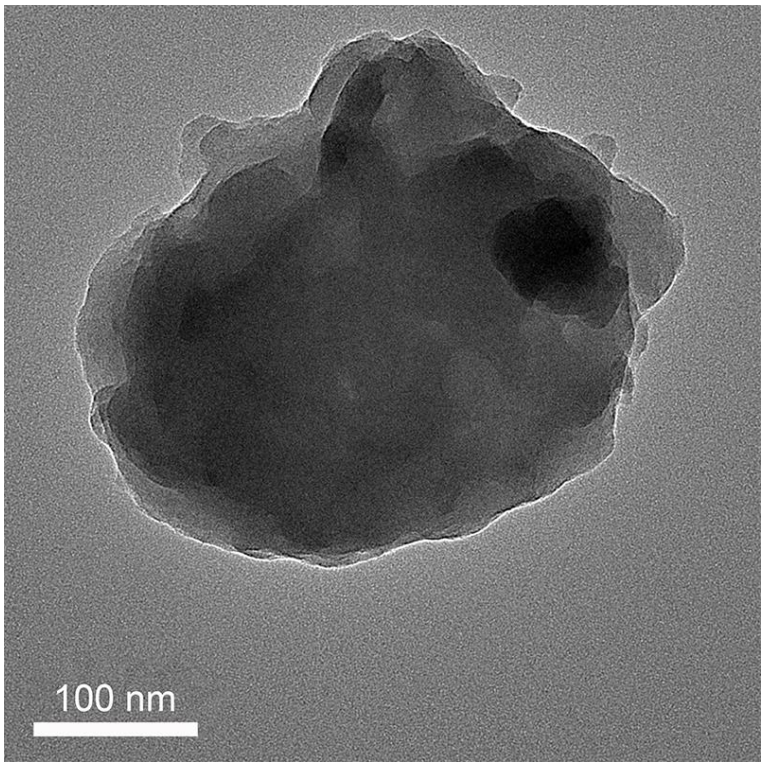

Supplementary Fig. 26 | TEM image of CuBBTA after electroreduction under Ar atmosphere.

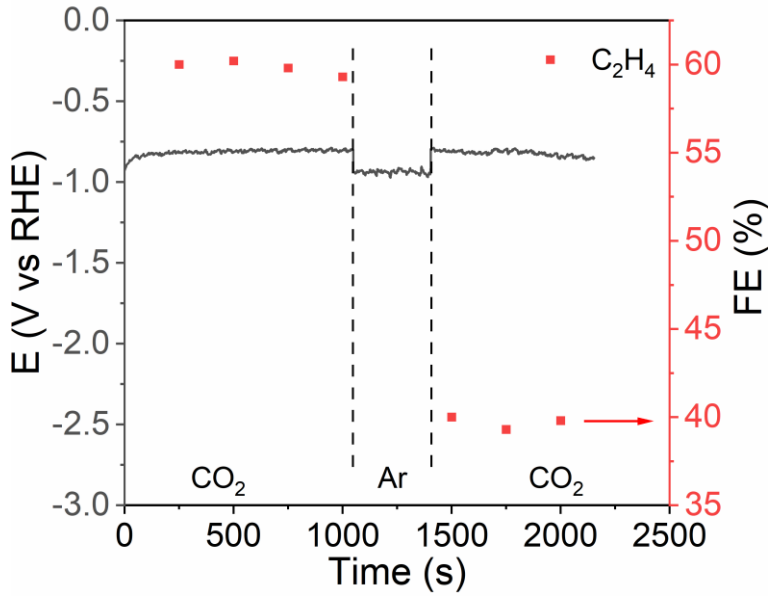

Supplementary Fig. 27 | The CO_2RR performance of CuBBTA at −300 mA cm^{-2} exhibited distinct trends under different atmospheres.

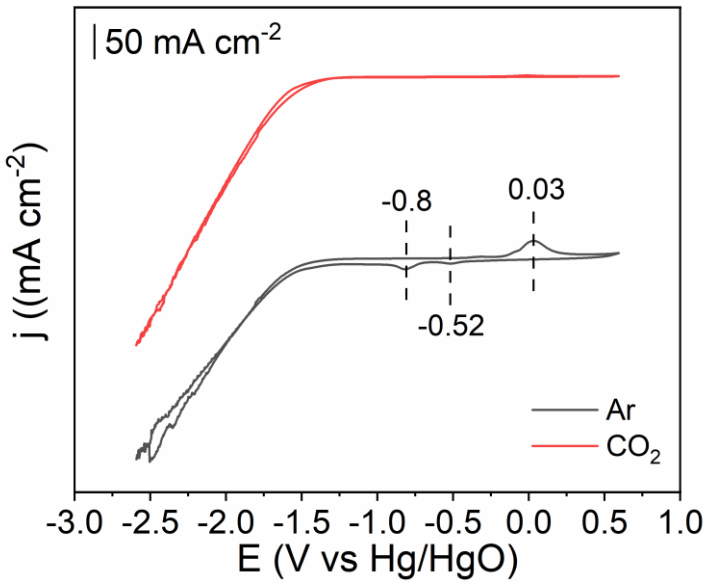

Supplementary Fig. 28 | Cyclic voltammetry (CV) curves of the CuBBTA electrode were recorded in 1 M KOH at a scan rate of 100 mV s^{-1} over a potential range of -2.5 V to 0.5 V (vs. Hg/HgO) under CO_2 and Ar atmospheres, respectively. Obvious reduction peak at -0.52 V (vs. Hg/HgO) (Cu^{2+} to Cu^{1+}) and -0.8 V (vs. Hg/HgO) (Cu^{2+} to Cu^0 and Cu^{1+} to Cu^0), and oxidation peak at 0.03 V (vs. Hg/HgO) (Cu^0 to Cu^{2+}) appeared under Ar atmosphere.[3-5]

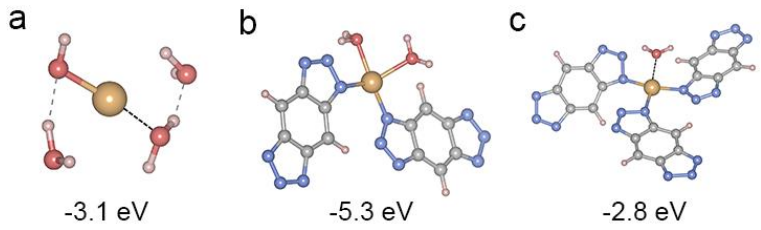

Supplementary Fig. 29 | DFT calculation of free energy of the intermediates were conducted as a reference during the formation of CuBBTA.

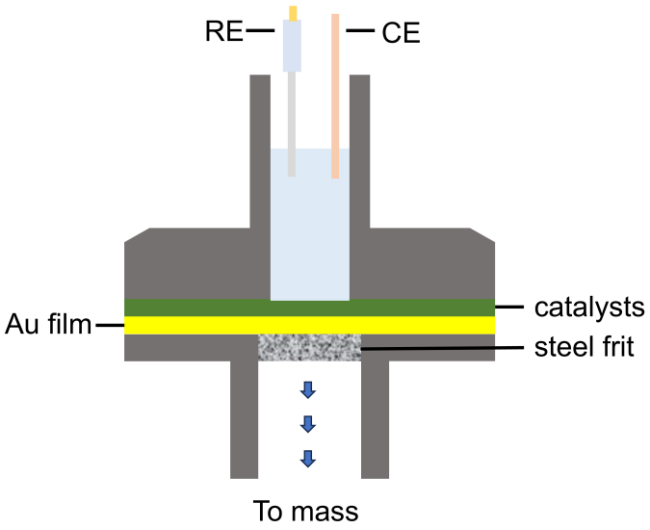

Supplementary Fig. 30 | Schematic illustration for DEMS measurement.

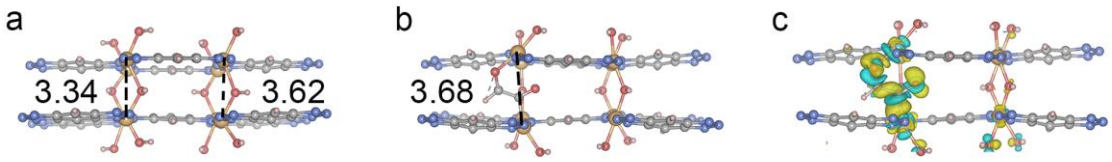

Supplementary Fig. 31 | DFT-predicted *COCHO configuration on CuBBTA and Cu-Cu distance before (a) and after (b) *CO/*CHO adsorption. (c) Top view of charge difference of *COCHO in CuBBTA slab. Cyan and yellow contours present electron depletion and electron accumulation, respectively. The iso-surface level is set to be 0.003 eV $Bohr^{-3}$.

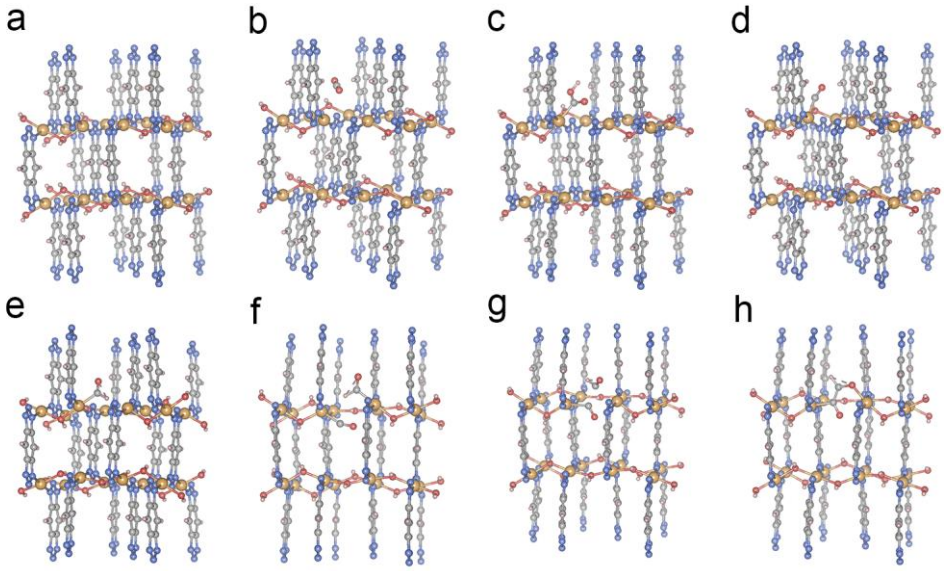

Supplementary Fig. 32 | The evolution of main intermediates from *CO_2 to *COCHO over CuBBTA during the CO_2 to C_2H_4 process. Side views of (a) CuBBTA; (b) *CO_2; (c) *COOH; (d) *CO; (e) *CHO (f) *CHO +*CO; (g) transition state of *COCHO; (h) *COCHO configurations.

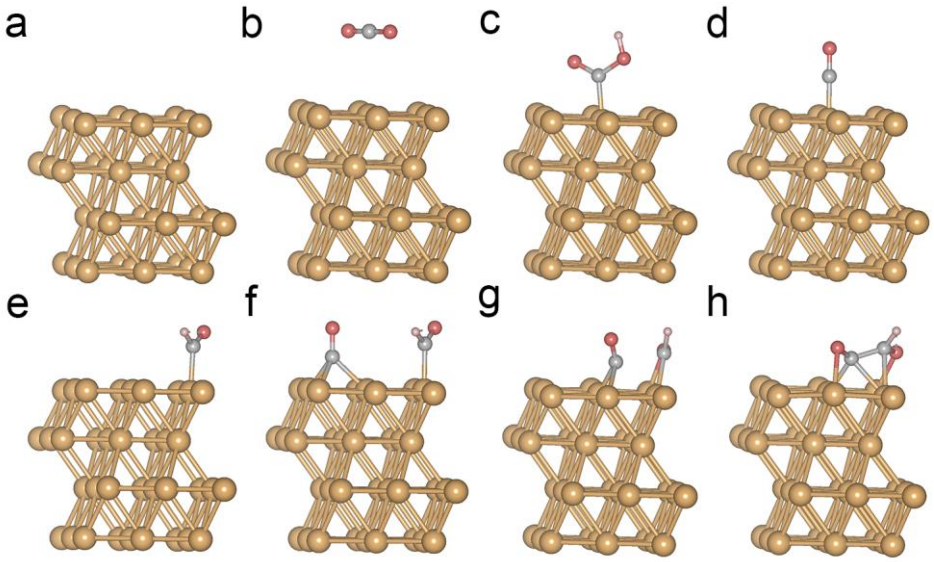

Supplementary Fig. 33 | The evolution of main intermediates from *CO_2 to *COCHO over Cu(111) during the CO_2 to C_2H_4 process. Side views of (a) Cu(111); (b) *CO_2; (c) *COOH; (d) *CO; (e) *CHO (f) *CHO +*CO; (g) transition state of *COCHO; (h) *COCHO configurations.

Supplementary Tables

Supplementary Table 1 | Summary of the amount of Cu in CuBBTA obtained by ICP-AES. The error bars for the data uncertainty represent one standard deviation based on three independent samples.

CuBBTA	Cu (Wt.%)[a]
1	38.8
2	40.2
3	39.2
average	39.4±0.7

[a]mass percentage.

Supplementary Table 2 | The metal loadings of selected Cu SACs from the available literature.

Sample	Synthetic strategy	Loading [wt%]	References
CuBBTA	One-pot synthesis approach	39.4	This Work
Cu/CN	Metal Coordination Route	16.3	[6]
CCPA	high-concentration precursors strategy	13-15	[7]
Cu-SACs	General negative pressure annealing approach	29.8	[8]
UHDCu-N-C SACs	metal sulfide-mediated atomic trapping	26.9	[9]
Cu_1/PCN	Scalable two-step annealing method	21.8	[10]
Cu SA nanoforest	a micellar brush–derived soft nanoforest system to immobilize SAs	18	[11]
Cu–N–C	high temperature pyrolysis	20.9	[12]

Supplementary Table 3 | EXAFS fitting data at the Cu K-edge of CuBBTA.

Catalyst	Scatter path	CN_{EXAFS} /CN_{DFT}	R_{EXAFS}/R_{DFT} (Å)	ΔE0 (eV)	σ^2 (Å^2)
CuBBTA	Cu-O	2.2±0.3/2.0	1.88±0.12/1.76	3.3±1.8	0.006±0.001
	Cu-N	2.0±0.4/2.0	2.01±0.05/1.98	6.9±4.7	0.008±0.002

CN_{DFT}: coordination numbers calculated by DFT. R_{DFT}: bond distance calculated by DFT. CN_{EXAFS}: coordination numbers simulated by E_{XAFS} fitting. R_{EXAFS}: bond distance simulated by E_{XAFS} fitting. σ^2: the Debye-Waller factor. ΔE_0: the inner potential shift. S_0^2 was fixed as 1. data ranges:2.5≤k≤12 Å^{-1},1.0≤R≤3.0. R factor for this fit is 1.5%.

Supplementary Table 4 | Element analysis of CuBBTA. The error bars for the data uncertainty represent one standard deviation based on three independent samples.

Elements	Calc.[a]	Found[a]
C(%)	22.57	21.6±0.2
N(%)	26.33	25.6±0.5
H(%)	1.26	1.35±0.06

[a]mass percentage.

Supplementary Table 5 | Comparison of half-cell C_2H_4 power conversion efficiency (PCE) over CuBBTA and D-Cu under different applied potential.

catalysts	Applied potential (vs. RHE)	$PCE_{ethylene}$(%)
CuBBTA	-0.69	26.7
	-0.74	28.9
	-0.79	33.0
	-0.84	34.4
	-0.89	29.4
	-0.94	21.9
D-Cu	-0.69	13.0
	-0.74	16.1
	-0.79	17.7
	-0.84	19.5
	-0.89	20.0
	-0.94	21.5

Supplementary Table 6 | Performance comparison of state-of-the-art Cu-based catalysts for CO_2RR to C_2H_4 reported in the literature.

Catalyst	Potential (V vs. RHE)	EE (%)	Current density (mA cm^{-2})	Reference
CuBBTA	0.84	34.4	305.2	This work
Au NWs-P1	-1.1	28.6	70	[13]
Cu_2-C_2N	-1.4	23.5	318.5	[14]
$Cu^{\delta+}NCN$	-1.4	31.7	∽400	[15]
Ln-Cu	-0.95	26.9	∽350	[16]
Cu-DEA-KB	-1.1	24.9	155.7	[17]
Cu2	-1.6	20.7	∽225	[18]
Cu_3N-Ag	-1	20	26.7	[19]
$Cu@C_{C=O,1}$	-0.93	35.4	295	[20]
Cu_1Ni-BDP	-1.3	24	279	[21]
TA−Cu	-1.2	30	316.2	[22]

Supplementary Table 7 | EXAFS fitting parameters for the Cu K-edge of the CuBBTA (S_0^2=0.86)

	shell	CN	R(Å)	σ^2	ΔE0
Pristine	Cu-N/O	4.0±0.7	1.86±0.02	0.006±0.001	8.2±0.8
OCP	Cu-N/O	4.1±0.6	1.78±0.01	0.003±0.001	8.7±0.6
-0.6 V	Cu-N/O	3.9±0.5	1.84±0.02	0.008±0.002	7.9±0.8
-0.7 V	Cu-N/O	4.2±0.6	1.92±0.02	0.005±0.001	9.5±1.2
-0.8 V	Cu-N/O	4.0±0.4	1.90±0.04	0.006±0.001	8.8±0.9
-0.9 V	Cu-N/O	3.8±0.6	1.86±0.03	0.004±0.001	9.2±0.6
-1 V	Cu-N/O	4.0±0.7	1.76±0.04	0.004±0.001	8.2±1.1
-1.1 V	Cu-N/O	4.1±0.5	1.85±0.01	0.007±0.001	8.0±0.8

Data ranges:2.5≤k≤12 $Å^{-1}$,1.0≤R≤3.0. R factor for this fit is 1.5%.

Supplementary Table 8 | Peak assignments of CuBBTA in Raman spectroscopy.[23]

Raman shift (cm^{-1})	Vibrational assignments
1625	[vCC +σHCC] in benzene
1559	vNC in triazole + vCC in benzene
1446	vNC in triazole
1332	σHCC
1280	vCC in triazole
1212	vCC in benzene + vCC in triazole
1205	vNN in triazole
775	σCCC
737	λHCCC
679	vNN in triazole

Abbreviations in the table: v, stretching; σ, in-plane bending; λ, torsion.

References

1. Ma H*, et al.* Study of cyano and hydroxyl groups modification on the properties of porous carbon nitride synthesized by using a salt assistant method. *Applied Surface Science* **507**, 144885 (2020).
2. Zhu H-L, Chen H-Y, Han Y-X, Zhao Z-H, Liao P-Q, Chen X-M. A porous π–π stacking framework with dicopper (I) sites and adjacent proton relays for electroreduction of CO_2 to C_{2+} products. *Journal of the American Chemical Society* **144**, 13319-13326 (2022).
3. Liu Q, Jiang Q, Li L, Yang W. Spontaneous reconstruction of copper active sites during the alkaline CORR: degradation and recovery of the performance. *Journal of the American Chemical Society* **146**, 4242-4251 (2024).
4. Basera P*, et al.* The Role of Cu^{3+} in the Oxygen Evolution Activity of Copper Oxides. *Journal of the American Chemical Society* **147**, 16070-16083 (2025).
5. Yang B*, et al.* Electrocatalytic CO_2 reduction to alcohols by modulating the molecular geometry and Cu coordination in bicentric copper complexes. *Nature Communications* **13**, 5122 (2022).
6. Duan Y*, et al.* Large-Scale Synthesis of High-Loading Single Metallic Atom Catalysts by a Metal Coordination Route. *Advanced Materials* **36**, 2404900 (2024).
7. Ma Z*, et al.* Conjugated Coordination Polymer Aerogels with Increased Accessibility of Well-Defined Single-Atom Metal Sites as a New Paradigm of Electrocatalysts. *Advanced Materials* **37**, 2420565 (2025).
8. Wang Y*, et al.* General negative pressure annealing approach for creating ultra-high-loading single atom catalyst libraries. *Nature Communications* **15**, 5675 (2024).
9. Chang J*, et al.* Synthesis of ultrahigh-metal-density single-atom catalysts via metal sulfide-mediated atomic trapping. *Nature Synthesis* **3**, 1427-1438 (2024).
10. Hai X*, et al.* Scalable two-step annealing method for preparing ultra-high-density single-atom catalyst libraries. *Nature nanotechnology* **17**, 174-181 (2022).
11. Sun Y*, et al.* Soft nanoforest of metal single atoms for free diffusion catalysis. *Science Advances* **11**, eadq2948 (2025).
12. Li F*, et al.* Boosting oxygen reduction catalysis with abundant copper single atom active sites. *Energy & Environmental Science* **11**, 2263-2269 (2018).
13. Chen Y*, et al.* N-Heterocyclic Carbene Polymer-Stabilized Au Nanowires for Selective and Stable Reduction of CO_2. *Journal of the American Chemical Society* **147**, 14845-14855 (2025).
14. Sun Z, Luo X, Shang H, Wang Z, Zhang L, Chen W. Atomic Printing Strategy Achieves Precise Anchoring of Dual-Copper Atoms on C_2N Structure for Efficient CO_2 Reduction to Ethylene. *Angewandte Chemie International Edition* **136**, e202405778 (2024).
15. Yue K*, et al.* Stabilized Cu^0-Cu^{1+} dual sites in a cyanamide framework for selective CO_2 electroreduction to ethylene. *Nature Communications* **15**, 7820

(2024).
16. Yang Y*, et al.* Ligand-tuning copper in coordination polymers for efficient electrochemical C–C coupling. *Nature communications* **15**, 6316 (2024).
17. Lv *Z, et al.* Enhanced CO_2 Adsorption and Conversion in Diethanolamine-Cu Interfaces Achieving Stable Neutral Ethylene Electrosynthesis. *Advanced Energy Materials* **14**, 2402551 (2024).
18. Chen S*, et al.* Copper atom pairs stabilize *OCCO dipole toward highly selective CO_2 electroreduction to C_2H_4. *Angewandte Chemie International Edition* **63**, e202411591 (2024).
19. Li J*, et al.* Cascade dual sites modulate local CO coverage and hydrogen-binding strength to boost CO_2 electroreduction to ethylene. *Journal of the American Chemical Society* **146**, 5693-5701 (2024).
20. Zhang T*, et al.* Active Oxygenated Structure-Intensified CO_2 Capture Enables Efficient Electrochemical Ethylene Production Over Carbon Nanofibers. *Angewandte Chemie International Edition* **136**, e202401707 (2024).
21. Huang L*, et al.* Enhanced CO_2 electroreduction selectivity toward ethylene on pyrazolate-stabilized asymmetric Ni–Cu hybrid sites. *Journal of the American Chemical Society* **145**, 26444-26451 (2023).
22. Chen S*, et al.* Selective CO_2 reduction to ethylene mediated by adaptive small-molecule engineering of copper-based electrocatalysts. *Angewandte Chemie International Edition* **135**, e202315621 (2023).
23. Thomas S, Venkateswaran S, Kapoor S, D'Cunha R, Mukherjee T. Surface enhanced Raman scattering of benzotriazole: A molecular orientational study. *Spectrochimica Acta Part A: Molecular and Biomolecular Spectroscopy* **60**, 25-29 (2004).